Inorganic Chemistry

Article

pubs.acs.org/IC

Electronic, Optical, and Computational Studies of a Redox-Active Napthalenediimide-Based Coordination Polymer

Chanel F. Leong,[†] Bun Chan,[†,‡] Thomas B. Faust,[†] Peter Turner,[†] and Deanna M. D'Alessandro*[,†]

[†]School of Chemistry, The University of Sydney, Sydney, New South Wales 2006, Australia

[‡]ARC Centre of Excellence for Radical Chemistry and Biotechnology, School of Chemistry, The University of Sydney, Sydney, New South Wales 2006, Australia

Supporting Information

ABSTRACT: The new one-dimensional coordination framework $(Zn(DMF)NO_3)_2(NDC)(DPMNI)$, where NDC = 2,6-naphthalenedicarboxylate and DPMNI = *N*,*N*′-bis(4-pyridylmethyl)-1,4,5,8-naphthalenetetracarboxydiimide, which has been crystallographically characterized, exhibits two redox-accessible states due to the successive reduction of the naphthalenediimide (NDI) ligand core. Solid-state electrochemical and vis−near-IR spectroelectrochemical measurements coupled with density functional theory (DFT) calculations enabled the origins of the optical transitions in the spectra of the monoradical anion and dianion states of the material to be assigned. Electron paramagnetic resonance (EPR) spectroscopy revealed that the paramagnetic radical anion state of the DPMNI core could be accessed upon broad-spectrum white light irradiation of the material, revealing a long-lived excited state, possibly stabilized by charge delocalization which arises from extensive $\pi-\pi^*$ stacking interactions between alternating NDC and NDI aromatic cores which are separated by a distance of 3.580(2) Å.

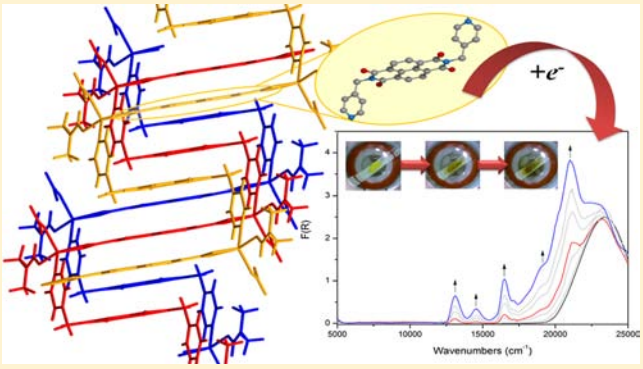

INTRODUCTION

The integration of redox-active components into coordination polymers and metal−organic frameworks paves the way toward novel materials which hold promise as solid-state conductors, electrocatalysts, and solar energy conversion devices among others.[1] In such materials, $\pi-\pi^*$ stacking of highly aromatic, redox-active ligand moieties is commonly observed, serving as both a means of structural stabilization and an avenue for electron transfer. Hence, pre-emptive design of the ligand cores, namely by the strategic incorporation of highly aromatic donors or acceptors, coupled with core functionalization, yields materials with tunable electronic and optical properties.[2,3] At a fundamental level, understanding the electronic and optical properties of coordination polymers underpins the theoretical understanding of electron migration in extended, multidimensional, and supramolecular systems.

A key requirement for practical application of these materials is their structural integrity in different redox states. Toward this goal, the incorporation of redox-active ligands into coordination polymers offers a potentially more viable route in comparison with redox activity based on the metal centers, as the latter are often predisposed to changes in coordination geometry upon redox state switching, leading to degradation of the overall extended framework structure.

In the present work, a combined methodology including solid-state electrochemical, spectroelectrochemical, and EPR techniques in addition to DFT computational methods is employed to interrogate the fundamental electronic and spectral properties of a novel one-dimensional coordination solid, $(Zn(DMF)NO_3)_2(NDC)(DPMNI)$, incorporating the flexible, redox-active naphthalenediimide-based ligand *N*,*N*′-bis(4-pyridylmethyl)-1,4,5,8-naphthalenetetracarboxydiimide (DPMNI), where NDC = 2,6-napthalenedicarboxylate.

The redox-active naphthalenediimide (NDI) core has been extensively studied both as a discrete unit and as a structural motif in extended one-, two-, and three-dimensional structures.[4−7] Such aromatic diimides are known to possess stable radical anion and dianion states,[5,8] which once ligated may produce extended conductive materials. In the present case, the application of a new technique for vis−near-IR spectroelectrochemistry[7] provides access to all redox states of the coordination framework, enabling unambiguous determination of the properties of the radical frameworks. In situ light irradiated electron paramagnetic resonance (EPR) spectroscopy is also employed to investigate the potential for photogeneration of these paramagnetic radical states of the material. The application of DFT computational calculations to a model fragment of the extended network enables the salient spectral features of the coordination framework to be elucidated, demonstrating the significance of employing complementary experimental and computational strategies to coordination

Received: August 26, 2013
Published: November 27, 2013

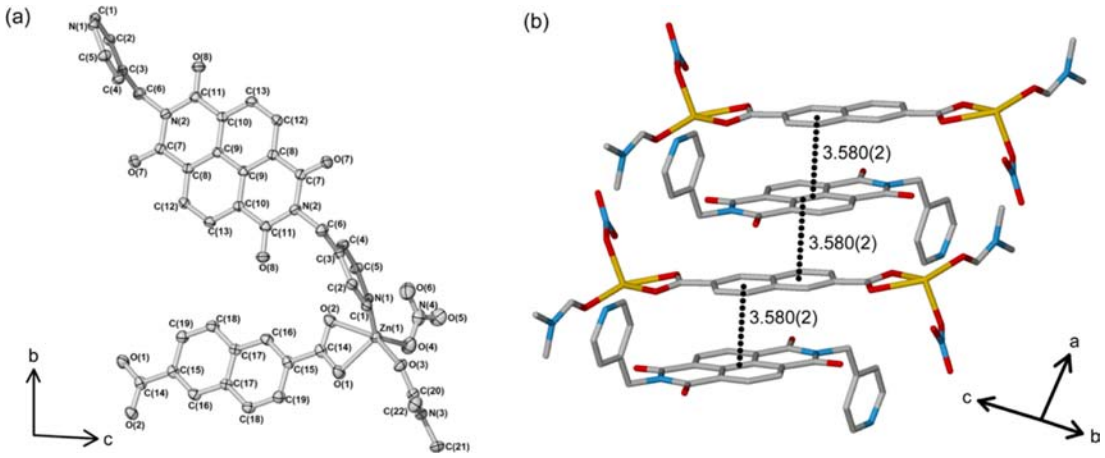

Figure 1. (a) ORTEP representation of the coordination environment around Zn^{2+} in $(Zn(DMF)NO_3)_2(NDC)(DPMNI)$ shown at 50% probability and (b) capped-stick representation of the $\pi-\pi^*$ stacking between the NDI and NDC moieties in the order ···NDC···NDI···NDC···NDI··· . Hydrogen atoms are omitted for clarity. Color scheme: Zn, yellow; C, gray; O, red; N, blue.

frameworks. This approach to understanding the fundamental properties of framework solids will underpin their development for future applications in the area of optoelectronics devices.

EXPERIMENTAL SECTION

Synthesis of *N,N′*-Bis(4-pyridylmethyl)-1,4,5,8-naphthalenetetracarboxydiimide (DPMNI). DPMNI was synthesized by an adaptation of literature methods.[9] 1,4,5,8-Naphthalenetetracarboxylic dianhydride (1.23 g, 4.6 mmol) and 4-(aminomethyl)pyridine (1.16 mL, 11.5 mmol) were refluxed in anhydrous DMF (20 mL) under N_2 for 12 h, yielding an orange-brown suspension. The solid was isolated by vacuum filtration and washed with dichloromethane and acetone prior to drying in vacuo. Yield: 1.48 g, 3.30 mmol, 89%. Mp: 333 °C. ^{1}H NMR (300 MHz, CF_3COOD): δ 8.94 (d, 4H), 8.77 (d, J = 6.0 Hz, 4H), 8.24 (d, J = 6.0 Hz, 4H), 5.78 (s, 4H). Anal. Calcd for $C_{26}H_{16}N_4O_4$ (M_w = 424.44): C, 69.6; H, 3.60; N, 12.5. Found: C, 69.7; H, 3.58; N, 12.6.

Synthesis of $(Zn(DMF)NO_3)_2(NDC)(DPMNI)$. A mixture of $Zn(NO_3)_2{\cdot}6H_2O$ (595 mg, 2.0 mmol), H_2NDC (87 mg, 0.40 mmol), and DPMNI (180 mg, 0.43 mmol) in DMF (200 mL) was heated for 2 days at 80 °C with stirring. A bright yellow, crystalline powder was isolated by filtration from the yellow mother liquor and washed with DMF prior to drying in vacuo. Yield: 190 mg, 0.18 mmol, 45% based on H_2NDC.

Single crystals of $(Zn(DMF)NO_3)_2(NDC)(DPMNI)$ suitable for single-crystal X-ray diffraction analysis were synthesized at one-tenth the scale of the bulk synthesis. The reagents were introduced into a 21 mL glass vial which was placed in an aluminum-lined heating block without agitation for 2 days at 80 °C. Yellow, tablet-shaped crystals were obtained. Anal. Calcd for $C_{80}H_{56}O_{29}N_8Zn_2$: C, 55.7; H, 3.27; N, 6.50. Found: C, 55.8; H, 3.26; N, 6.79.

General Characterization Methods. The ^{1}H NMR spectrum of DPMNI was collected using a Bruker AVANCE III 300 MHz spectrometer. Elemental analyses were determined at the Chemical Analysis Facility at Macquarie University. Each sample was dried at 110 °C for 16 h prior to analysis and was run in duplicate. Powder X-ray diffraction (PXRD) data were obtained using a PANalytical XPert PRO diffractometer equipped with a solid-state PIXcel detector employing Cu Kα (λ = 1.5406 Å) radiation. Thermogravimetric analysis (TGA) was performed on a TA Instruments Hi-Res TGA 2950 instrument, heating to 600 °C at a ramp rate of 2 °C min^{-1} under a flow of N_2 (0.1 L min^{-1}). FTIR spectra were collected using a Bruker Tensor 27 infrared spectrometer. Samples were prepared in a dry, finely ground potassium bromide (KBr) matrix. A background scan of KBr was collected prior to each analysis. Data were collected within the range 4000−400 cm^{-1}.

Single-Crystal X-ray Crystallography of $(Zn(DMF)NO_3)_2(NDC)(DPMNI)$. A yellow tablet-shaped crystal was attached with Exxon Paratone N to a short length of fiber supported on a thin piece of copper wire inserted in a copper mounting pin. The crystal was quenched in a cold nitrogen gas stream from an Oxford Cryosystems Cryostream. An Agilent SuperNova Dual diffractometer equipped with an Atlas detector and employing mirror-monochromated Cu Kα radiation (λ = 1.5418 Å) from a microsource was used for the data collection. Cell constants were obtained from a least-squares refinement against 13537 reflections located between 10 and 152° 2θ. Data were collected at 150(2) K with ω scans to 153° 2θ. The data processing was undertaken with CrysAlis Pro,[10] and subsequent computations were carried out with WinGX[11] and ShelXle.[12] A multiscan absorption correction was applied to the data.[10]

The structure was solved in the space group $P\bar{1}$ (No. 2) by direct methods with SIR97[13] and extended and refined with SHELXL-97.[14] The structure is oligomeric, and the two bridging ligands are each located on inversion centers ($1-x, -y, -z$ and $-x, 2-y, -z$). The non-hydrogen atoms in the asymmetric unit were modeled with anisotropic displacement parameters, and a riding atom model with group displacement parameters was used for the hydrogen atoms. An ORTEP[15] depiction of the molecule with 50% displacement ellipsoids is provided in Figure 1.

Crystal data: formula $C_{22}H_{18}N_4O_8Zn$, M 531.77, triclinic, space group $P\bar{1}$ (No. 2), a = 7.5108(2) Å, b = 8.1831(2) Å, c = 17.6865(4) Å, α = 92.283(2)°, β = 94.663(2)°, γ = 97.343(2)°, V = 1073.17(5) Å^3, D_c = 1.646 g cm^{-3}, Z = 2, crystal size 0.153 × 0.097 × 0.026 mm, color yellow, habit tablet, temperature 150(2) K, λ(Cu Kα) = 1.5418 Å, λ(Cu Kα) = 2.125 mm^{-1}, T_{min}, T_{max} = 0.872, 1.000, $2\theta_{max}$ = 153.02, hkl range −9 to + 8, −10 to +10, −22 to +22, N = 34241, N_{ind} = 4493 (R_{merge} = 0.0398), N_{obs} = 4074 ($I > 2\sigma(I)$), N_{var} = 306, residuals R1(F) = 0.0336, wR2(F^2) = 0.0993, GOF(all) = 1.451, $\Delta\rho_{min}$, $\Delta\rho_{max}$ −0.351, 0.543 e Å^{-3}. Note: R1 = $\sum||F_o| - |F_c||/\sum|F_o|$ for $F_o > 2\sigma(F_o)$; wR2 = $(\sum w(F_o^2 - F_c^2)^2/\sum(wF_c^2)^2)^{1/2}$ for all reflections; $w = 1/[\sigma^2(F_o^2) + (0.05P)^2P]$, where $P = (F_o^2 + 2F_c^2)/3$. CCDC deposition number 956802.

Solid-State Electrochemistry. Solid-state cyclic voltammetry (CV) was performed using a BASi Epsilon Electrochemical Analyzer. Measurements were conducted under an inert Ar atmosphere using a conventional three-electrode cell with a glassy-carbon working electrode to which the sample was immobilized, a Pt-wire auxiliary electrode, and an Ag/Ag^+ quasi-reference electrode. A 0.1 M tetrabutylammonium hexafluorophosphate n-Bu_4NPF_6/CH_3CN electrolyte was employed, scanning at a rate of 500 mV/s. Potentials were referenced to the Fc^0/Fc^+ couple.

Photoirradiated Electron Paramagnetic Resonance (EPR) Spectroscopy. Continuous-wave EPR measurements were collected on a Bruker EMX X-band spectrometer at room temperature. Samples

dx.doi.org/10.1021/ic402173z | Inorg. Chem. 2013, 52, 14246−14252

were loaded into quartz capillary tubes (4 mm diameter). Specific parameters of the dark scan are as follows: receiver gain, 1.00×10^5; modulation frequency, 100 kHz; modulation amplitude, 1.00 G; sweep width, 50 G; resolution, 1024 points; conversion, 40.960 ms; sweep time, 41.943 s. Specific parameters of the irradiated sample scan are as follows: receiver gain, 5.02×10^4; modulation frequency, 100 kHz; modulation amplitude, 5.00 G; sweep width, 40 G; resolution, 1024 points; conversion, 81.920 ms; sweep time, 83.886 s. Photoirradiation was performed by directing a broad-spectrum white light through the sample cavity grating (approximately 30% transmittance) for 10 min and collecting single scans to follow the signal decay with time.

Solid-State Spectroelectrochemistry (SEC). Visible−near-infrared (vis−near-IR) data were collected using a CARY5000 spectrometer equipped with a Harrick Omni Diff Probe attachment. Electrochemical experiments were performed in a Teflon SEC cell comprising two side arms separately accommodating a platinum-wire auxiliary electrode and an Ag/Ag^+ wire quasi-reference electrode.[7] These side arms connect at a central compartment that harbors a 0.1 M n-Bu_4NPF_6/CH_3CN electrolyte. The sample was affixed to an indium−tin oxide (ITO) coated quartz slide (working electrode) by a strip of Teflon tape, and the circuit was completed with conductive copper adhesive tape. This slide was inverted over the central compartment to enable contact between the sample and electrolyte, and was finally fixed with adhesive tape. A baseline scan of the Teflon tape was collected from 5000 to 25000 cm^{-1}. Potentials were controlled using an eDAQ e-corder 410 potentiostat. Continuous scans of the sample were undertaken at a potential of 0 V until spectral equilibration was achieved. A cathodic potential was then manually applied incrementally during a cycled collection where time was given for spectral equilibration before a more cathodic potential was applied.

Gas Adsorption Measurements. Pure gas adsorption measurements were conducted using a Micromeritics 2020 Accelerated Surface Area and Porosimetry System (ASAP). The solid (66.8 mg) was degassed via a temperature program of 2 °C min^{-1} to 80 °C followed by 1 °C min^{-1} to 140 °C, where it was held for at least 6 h prior to analysis. Surface area measurements were obtained at 77 K via incremental dosing of N_2 from 0 to 1 bar, and the Brunauer−Emmett−Teller (BET) surface area was determined through the use of the ASAP 2020 V4.01 software.

Computational Methods. Standard density functional theory (DFT) calculations were carried out with Gaussian 09.[16] The geometry of the model was extracted from the crystal structure of the coordination polymer, primarily without modification. The carboxylates in the NDC moiety were capped with Li^+ ions (at the location of the Zn^{2+} atoms) for the purpose of charge balance. This choice of capping is based on the similar sizes of Li (1.45 Å) and Zn (1.35 Å). For the napthalenediimide moiety, the terminal N−H bond lengths were optimized at the B3-LYP/6-31G(d) level.

These models were embedded in a continuum to approximate the effect of crystal packing in the solid, which is similar to the approach used by McCarthy et al.[2] to model a related metal−organic framework. The SMD continuum model[17] was used in conjunction with M05-2X/6-31G(d),[18] which is a method recommended for use with the SMD model. The parameters for benzene were employed in the SMD calculations to reflect the solid-state environment that is rich in aromatic moieties. We note that the dielectric constant of benzene is 2.27, which is close to the value of 2 employed by McCarthy et al.

The TD-BMK/6-31G(d) procedure[19] was employed to compute the vis−near-IR spectra of the model system. We note that BMK is one of the best-performing DFT methods for the computation of electronic transitions, as found by Goerigk and Grimme[20] in a comprehensive benchmark study. Nonetheless, BMK has a slight tendency to overestimate excitation energies (in general, by ∼900 cm^{-1}). We also note that the use of the 6-31G(d) basis set is likely to lead to an overestimation of excitation energies in comparison with results obtained with larger triple-ζ basis sets. In the closely related system of McCarthy et al., this difference is ∼600 cm^{-1}.[2] In our preliminary benchmark study on related aromatic diimides, we found a notably larger deviation (blue shift) for higher-energy transitions (>20000 cm^{-1}) with TD-BMK/6-31G(d) (Supporting Information, Figure S12). Thus, a total correction of −1500 cm^{-1} was applied to the TD-BMK/6-31G(d) spectra for low-energy transitions (<20000 cm^{-1}) and −3000 cm^{-1} for bands >20000 cm^{-1}. The simulated spectra were modeled by Gaussian functions with a half-width of 500 cm^{-1}, which is comparable to the resolution of the experimental spectra. Assignment of the molecular orbitals involved in the transitions was based on the dominant contribution to each excited state and the visualization of the associated orbitals (Supporting Information, Table S7).

RESULTS AND DISCUSSION

The crystal structure of $(Zn(DMF)NO_3)_2(NDC)(DPMNI)$ was determined using X-ray diffraction data collected at 150 K from single crystals obtained at 80 °C. The structure features one-dimensional coordination polymers comprised of distorted-trigonal-bipyramidal Zn^{2+} centers coordinated to one DMF molecule and one NO_3^- anion (via their oxygen atoms), a single DPMNI ligand via the pyridyl nitrogen, and an NDC ligand via chelation of the carboxylate group, as shown in Figure 1a (crystallographic information is provided in the Supporting Information). Adjacent chains are closely packed by virtue of $\pi-\pi^*$ stacking of alternating NDC and DPMNI aromatic cores which are separated by a distance of 3.580(2) Å (Figure 1b), forming layers on the (001) planes. The dense packing of the 1-D chains due to $\pi-\pi^*$ stacking between the DPMNI and NDC ligand cores of neighboring chains results in no solvent-accessible pore volume, as confirmed via PLATON. This is in agreement with the low BET surface area of 22.0 ± 0.2 m^2 g^{-1} determined from the N_2 adsorption isotherm collected at 77 K, which is indicative of surface adsorption, and the minimal CO_2 uptake at 298 K (Supporting Information).

Le Bail refinement of the PXRD pattern obtained from a bulk sample of the as-synthesized framework at 298 K was in good agreement with the single-crystal data, whereby the fitted unit cell parameters of a = 7.728(2) Å, b = 8.024(2) Å, and c = 17.524(4) Å at 298 K are very similar to those determined from the single-crystal data at 150 K (Supporting Information).

Thermogravimetric analysis revealed an approximately 11% weight loss in the region 140−200 °C due to DMF (Supporting Information), which was in reasonable agreement with the DMF content of the crystal structure (14% by mass). Attempts to exchange the coordinated DMF molecules for lower boiling point solvents such as methanol, ethanol, THF, and $CHCl_3$, led to a loss of crystallinity which may result from weakening of the intermolecular interactions between adjacent chains and the destruction of the crystal structure. Indeed, the persistence of the characteristic DMF ν(C═O) stretching frequency (Supporting Information) suggests that the DMF molecules remain coordinated to the Zn^{2+} metal centers following the attempted solvent exchange procedures.

Solid-state cyclic voltammetry was performed on $(Zn(DMF)NO_3)_2(NDC)(DPMNI)$ as a microcrystalline powder which was mechanically immobilized onto a glassy-carbon-disk working electrode. The voltammogram revealed two reduction processes at −0.85 and −1.30 V vs Fc^0/Fc^+ at 500 mV/s, which are characteristic of the formation of the monoradical anion and dianion forms of the DPMNI ligand (Figure 2).[8] These data are consistent with previous results for ligands containing the redox-active NDI core.[5,6] Due to poor diffusivity of counterions through the material as a result of dense packing, the redox processes observed via solid-state electrochemistry are likely to be localized at the surface of the crystallites. The reversibility of these processes is dependent on the transfer of counterions of opposite charge through the material to compensate for the

dx.doi.org/10.1021/ic402173z | Inorg. Chem. 2013, 52, 14246−14252

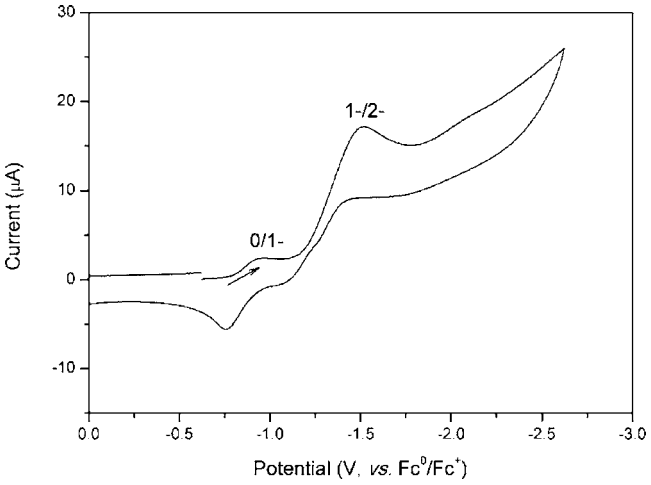

Figure 2. Solid-state cyclic voltammogram of $(Zn(DMF)NO_3)_2(NDC)(DPMNI)$ in 0.1 M n-Bu_4NPF_6/CH_3CN. Potentials are referenced to Fc^0/Fc^+. The arrow indicates the direction of the forward scan.

change in oxidation state of the ligand, and they are thus closely linked to the adsorption or desorption of counterion guests. A plot of the separation between the anodic and cathodic peak potentials for the first reduction process against the square root of the scan rate revealed a linear relationship, indicating that this is a quasi-reversible process governed by slow reaction kinetics (Supporting Information)[21] owing to the densely packed structure.

Solid-state EPR spectroscopy of $(Zn(DMF)NO_3)_2(NDC)(DPMNI)$ confirmed the absence of unpaired spins in the as-synthesized material (Figure 3) due to the diamagnetic nature

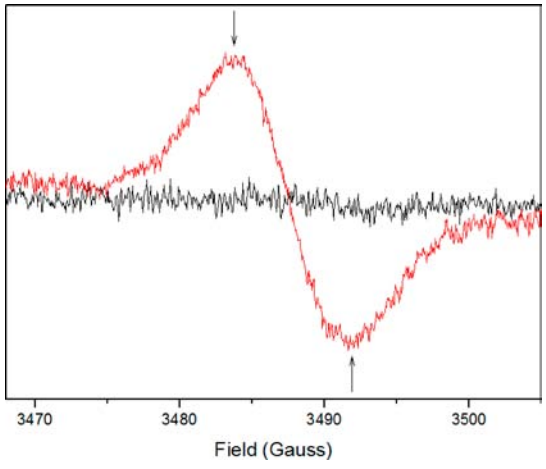

Figure 3. EPR spectrum of $(Zn(DMF)NO_3)_2(NDC)(DPMNI)$ prior to irradiation (black; 9.800 GHz, 6.377 mW) and after 5 min of irradiation with broad-spectrum white light (red; 9.829 GHz, 2.017 mW). The arrows show the direction of the decay of the NDI radical back to its neutral state.

of the d^{10} metal center and the neutral state of the NDC and DPMNI ligands. Interestingly, upon irradiation of the material with broad-spectrum white light for 5 min, a signal corresponding to g = 2.0056 was observed, suggesting that excitation of at least a fraction of NDI cores to their monoradical anion state has occurred. The signal did not intensify after 5 min of irradiation and decayed approximately 20 min after irradiation ceased. It is possible that this long-lived charge-separated state is stabilized by the extensive $\pi-\pi^*$ stacking interactions with NDC moieties, allowing for the delocalization of charge between the stacked cores. The low population of this excited state is likely to be a consequence of dense packing in the $(Zn(DMF)NO_3)_2(NDC)(DPMNI)$ structure, which only allows for surface excitation of crystallites. Furthermore, since the sample was irradiated in situ from one direction only, a significant proportion of the solid would not have been exposed to light (EPR tube internal diameter 3 mm).

Solid-state vis−near-IR spectroelectrochemical (SEC) measurements of $(Zn(DMF)NO_3)_2(NDC)(DPMNI)$ were employed to characterize the optical properties of the coordination polymer as a function of its redox state.[7] The initially yellow microcrystalline solid attained a brown coloration at an applied potential of −0.78 V, as evidenced by the gradual emergence of bands in the visible region of the spectrum between 14000 and 20000 cm^{-1} in Figure 4. These bands were absent in the neutral

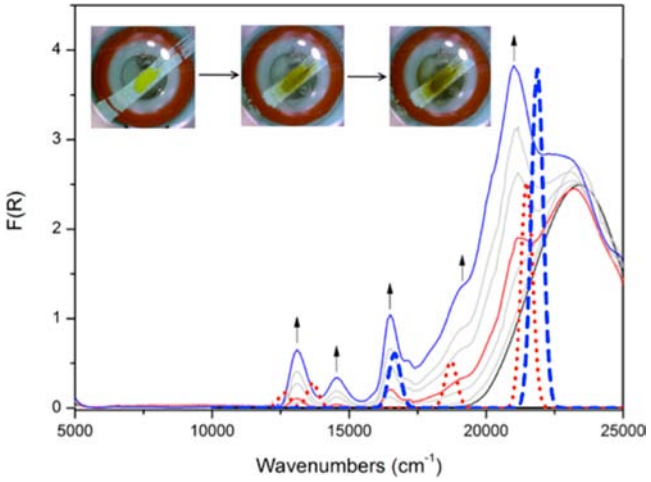

Figure 4. Solid-state vis−near-IR spectroelectrochemistry of $(Zn(DMF)NO_3)_2(NDC)(DPMNI)$ in 0.1 M n-Bu_4NPF_6/CH_3CN showing its neutral (black), monoradical (red), and dianion (blue) states. The dashed lines represent adjusted-theoretical spectra for the NDI-$NDCLi_2$ model compound, and the inset shows the change in color from yellow to brown upon reduction.

material at 0 V (black line) and are characteristic of the monoradical anion of the NDI ligand core (red line), as detailed in previous literature reports.[22] A rapid and significant increase in the intensities of the spectral bands across the visible region was observed as the potential was maintained at −0.78 V, resulting in a dark brown coloration of the material (depicted by the blue spectrum in Figure 4). The intensities of the bands continued to increase incrementally at a constant rate as the potential was further maintained at −2.20 V. A red shift of the band in the region 22500−25000 cm^{-1} was also observed upon reduction of the framework.

The spectroelectrochemical data are consistent with two redox processes in the framework which may be characterized as the reduction of the neutral material to the monoradical anion $(Zn(DMF)NO_3)_2(NDC)(DPMNI^{\bullet-})$ as depicted by the red spectrum in Figure 4, followed by reduction to the dianion $(Zn(DMF)NO_3)_2(NDC)(DPMNI^{2-})$, as depicted by the blue spectrum. In comparison to the electrochemical data for $(Zn(DMF)NO_3)_2(NDC)(DPMNI)$ shown in Figure 2, a potential slightly more cathodic than that required for the

dx.doi.org/10.1021/ic402173z | Inorg. Chem. 2013, 52, 14246−14252

second reduction process was employed in the SEC experiment due to the higher cell resistance.

To gain a deeper understanding of the electronic nature of $(Zn(DMF)NO_3)_2(NDC)(DPMNI)$, TD-DFT calculations were employed to model a representative molecular fragment of the coordination solid: specifically, an NDI−NDC complex. For charge balance, the two NDC carboxylates were capped with Li^+ (denoted NDI−$NDCLi_2$). In the present study, the spectroscopic properties of the monoradical anion and dianion species were of particular interest given that the UV−vis−near-IR spectra for the neutral framework $Zn_2(NDC)_2(DPNI)$ (where DPNI = *N*,*N*′-bis(4-pyridyl)-1,4,5,8-naphthalenetetracarboxydiimide), which is closely related to $(Zn(DMF)NO_3)_2(NDC)(DPMNI)$, have already been thoroughly investigated elsewhere.[2] TD-DFT calculations were thus employed to assign the species responsible for emergence of the low-energy bands in the visible region upon spectroelectrochemical reduction (Figure 4) and to identify the electronic features of the reduced species that correspond with the new transitions in the visible region of their spectra.

The computed vis−near-IR spectra for the model compounds, after the application of appropriate shifts (see the Experimental Section), are also shown in Figure 4 as dashed lines. Favorable agreement was found between the adjusted-theoretical and experimental spectra for the monoanion and dianion species, with minor deviations in energies for the calculated transitions lying within the typical deviation of ∼0.2 eV for TD-DFT calculations.[20] Accordingly, each of the low-energy visible bands which emerge upon reduction (Figure 4) are assignable to the monoanion or dianion species or both. Table 1 presents a summary of the nature of the transitions in these species and the assignment of the donor and acceptor orbitals.

Table 1. Spectral Assignments for the Monoanionic (1e) and Dianionic (2e) states of the NDI−$NDCLi_2$ Model Complex (Figure 4) According to TD-DFT Calculations, with the Percentage Contributions of the Assigned Orbitals Given in Parentheses (Figure 5)[a]

band (cm^{-1})	species	donor	acceptor
13100	1e	NDI-HOMO (88)	$NDCLi_2$-LUMO (82)
14600	1e	NDI-HOMO (88)	NDI-LUMO (61)
16500	2e	NDI-HOMO (84)	NDI-LUMO (68)
19000	1e	NDI-HOMO (88)	NDI-LUMO+1 (57)
20700	1e	$NDCLi_2$-HOMO (79)	NDI-HOMO (88)
	2e	NDI-HOMO (84)	NDI-LUMO+1 (57)

[a]HOMO and LUMO refer to the highest-occupied and lowest-unoccupied molecular orbitals within the designated fragment, which may differ from the HOMO and LUMO of the NDI−$NDCLi_2$ complex.

An examination of the calculated molecular orbitals for the NDI−$NDCLi_2$ model complex and its one- and two-electron reduced forms provided insight into the location of the reduction processes and the nature of the transitions in these systems. Figure 5 shows the HOMO and LUMO for the neutral model complex NDI−$NDCLi_2$ and the HOMO of the one- and two-electron reduced species. In neutral NDI−$NDCLi_2$, the HOMO is localized on the $NDCLi_2$ moiety, while the LUMO is localized on the NDI fragment. It is evident that, even for two-electron reduction, it is the NDI fragment, and specifically the LUMO of the neutral NDI moiety, that captures the additional negative charge. This is perhaps not surprising, as the $NDCLi_2$ fragment formally contains a dianion in the neutral complex.

The transitions in the experimental vis−near-IR spectra for $(Zn(DMF)NO_3)_2(NDC)(DPMNI)$ and its reduced forms were assigned by comparison with the calculated spectra for the NDI−$NDCLi_2$ model complex and its monoanion and dianion analogues. As shown in Table 1, the transitions in the visible region below 19000 cm^{-1} originate from the HOMO of the NDI fragment of the reduced complex. The energies of these transitions can be rationalized on the basis that the HOMO of the reduced NDI moiety was formerly an antibonding orbital, specifically the LUMO of the NDI fragment within the neutral NDI−$NDCLi_2$ complex. The energy gaps between bonding and antibonding orbitals are typically large; for example, the HOMO−LUMO gap in the neutral NDI−$NDCLi_2$ complex was calculated to be 31896 cm^{-1} (382 kJ mol^{-1}) at the BMK/6-31G(d) level. Therefore, these transitions would usually be of relatively high energy. On the other hand, the energy gaps between antibonding orbitals are typically smaller; for instance, the energy difference between the LUMO and LUMO+1 in the neutral form of NDI−$NDCLi_2$ is 15300 cm^{-1} (183 kJ mol^{-1}). The lower energies of the transitions in the reduced species relative to the neutral complex can thus be rationalized intuitively on the basis that they occur between "antibonding" orbitals.

CONCLUSIONS

The present study has sought to investigate electronic and optical properties of the coordination solid $(Zn(DMF)NO_3)_2(NDC)(DPMNI)$ using complementary experimental and computational approaches. The generation of the monoradical anion and dianion species of the material via in situ solid-state vis−near-IR spectroelectrochemistry has enabled the optical spectra of all three redox states to be unambiguously assigned by comparison with simulated spectra obtained from TD-DFT calculations. The information derived from this study confirmed that the monoradical anion and dianion states of the DPMNI moiety within the coordination solid are formed upon one- and two-electron reduction, and these are primarily responsible for the spectral features in the visible region of the electronic spectra. While no evidence for interchromophore charge transfer was found from either the experimental or computational data, the appearance of an EPR signal corresponding to g = 2.0056 upon light irradiation, in addition to the slow decay of this signal over a time period of minutes after irradiation ceased, suggests that a long-lived charge-separated state may be accessible in such coordination polymers where extensive $\pi-\pi^*$ stacking interactions are present.

The design of redox-active coordination polymers paves the way toward multifunctional systems which hold promise as conductors, sensors, and dynamic adsorbents.[23] The capacity to engineer conductivity, porosity, and redox activity into highly porous framework systems may also lead to their application in electrical swing adsorption for gas separations. Ultimately, understanding the fundamental electronic and optical properties of coordination polymers and metal−organic frameworks which incorporate components for electron transfer underpins the development of these materials for new applications.

dx.doi.org/10.1021/ic402173z | *Inorg. Chem.* 2013, 52, 14246−14252

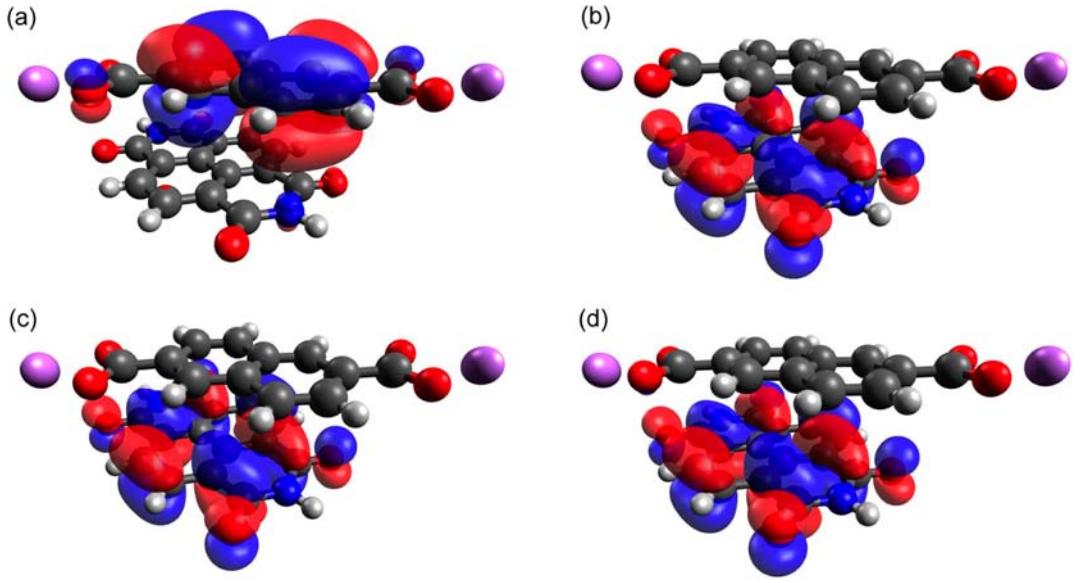

Figure 5. (a) HOMO and (b) LUMO of the neutral NDI−$NDCLi_2$ complex and the HOMO of (c) NDI−$NDCLi_2^{\bullet-}$ and (d) NDI−$NDCLi_2^{2-}$.

■ ASSOCIATED CONTENT

Supporting Information

Figures, tables and CIF files giving the structure of DPMNI, an ORTEP depiction of $(Zn(DMF)NO_3)_2(NDC)(DPMNI)$, relevant crystallographic details and an extended packing diagram, Le Bail refinement model of the bulk solid, TGA of as-synthesized $(Zn(DMF)NO_3)_2(NDC)(DPMNI)$, PXRD and FTIR overlay of solvent-exchanged material, CO_2 and N_2 adsorption isotherms at 298 K and N_2 isotherm at 77 K, rate-dependent cyclic voltammograms, sections of Gaussian output files relevant to the simulated vis−near-IR spectra, orbital energies for neutral NDI-$NDCLi_2$, and Cartesian coordinates for the NDI-$NDCLi_2$ complex used in the TD-DFT calculations. This material is available free of charge via the Internet at http://pubs.acs.org.

■ AUTHOR INFORMATION

Corresponding Author

*D.M.D.: e-mail, deanna@chem.usyd.edu.au; fax, +61 (2) 9351 3329; tel, +61 (2) 9351 3777.

Notes

The authors declare no competing financial interest.

■ ACKNOWLEDGMENTS

We gratefully acknowledge support from the Australian Research Council and the Science and Industry Endowment Fund and generous grants of computer time from the National Computational Infrastructure and Intersect Australia Ltd. We also thank Professor Mike Davies from the Heart Research Institute at The University of Sydney for generous access to a spectrometer for light-activated EPR measurements.

■ REFERENCES

(1) D'Alessandro, D. M.; Kanga, J. R. R.; Caddy, J. S. *Aust. J. Chem.* **2011**, *64* (6), 718−722. Kepert, C. J., Metal-Organic Framework Materials. In *Porous Materials*; Wiley: Chichester, U.K., 2010; pp 1−67. D'Alessandro, D. M.; Smit, B.; Long, J. R. *Angew. Chem., Int. Ed.* **2010**, *49* (35), 6058−6082.

(2) McCarthy, B. D.; Hontz, E. R.; Yost, S. R.; Van Voorhis, T.; Dinca, M. *J. Phys. Chem. Lett.* **2013**, *4* (3), 453−458.

(3) Martínez-Martínez, V.; Furukawa, S.; Takashima, Y.; López Arbeloa, I.; Kitagawa, S. *J. Phys. Chem. C* **2012**, *116* (49), 26084−26090.

(4) Bhosale, S. V.; Jani, C. H.; Langford, S. J. *Chem. Soc. Rev.* **2008**, *37* (2), 331−342. Pan, M.; Lin, X.-M.; Li, G.-B.; Su, C.-Y. *Coord. Chem. Rev.* **2011**, *255* (15−16), 1921−1936. Thalacker, C.; Röger, C.; Würthner, F. *J. Org. Chem.* **2006**, *71* (21), 8098−8105.

(5) Andric, G.; Boas, J. F.; Bond, A. M.; Fallon, G. D.; Ghiggino, K. P.; Hogan, C. F.; Hutchison, J. A.; Lee, M. A.; Langford, S. J.; Pilbrow, J. R.; Troup, G. J.; Woodward, C. P. *Aust. J. Chem.* **2004**, *57* (10), 1011−1019.

(6) Asir, S.; Demir, A. S.; Icil, H. *Dyes Pigm.* **2010**, *84* (1), 1−13.

(7) Usov, P. M.; Fabian, C.; D'Alessandro, D. M. *Chem. Commun.* **2012**, *48*, 3945−3947.

(8) Hamilton, D. G.; Montalti, M.; Prodi, L.; Fontani, M.; Zanello, P.; Sanders, J. K. M. *Chem. Eur. J.* **2000**, *6* (4), 608−617.

(9) Dinolfo, P. H.; Williams, M. E.; Stern, C. L.; Hupp, J. T. *J. Am. Chem. Soc.* **2004**, *126* (40), 12989−13001.

(10) *CrysAlisPro Version 1.171.35.11*; Agilent Technologies, Yarnton, Oxfordshire, U.K., 2011.

(11) Farrugia, L. J. *J. Appl. Crystallogr.* **1999**, *32*, 837−838.

(12) Hübschle, C. B.; Sheldrick, G. M.; Dittrich, B. *J. Appl. Crystallogr.* **2011**, *44*, 1281−1284.

(13) Altomare, A.; Burla, M. C.; Camalli, M.; Cascarano, G. L.; Giacovazzo, C.; Guagliardi, A.; Moliterni, A. G. G.; Polidori, G.; Spagna, R. J. *J. Appl. Crystallogr.* **1998**, *32*, 115−119.

(14) Sheldrick, G. M. *SHELX97 Programs for Crystal Structure Analysis*; Institüt für Anorganische Chemie der Universität, University of Göttingen, Tammanstrasse 4, D-3400 Göttingen, Germany, 1998.

(15) Johnson, C. K. *ORTEPII*; Report ORNL-5138, Oak Ridge National Laboratory, Oak Ridge, TN, 1976. Hall, S. R.; du Boulay, D. J.; Olthof-Hazekamp, R. *Xtal3.6 System*; University of Western Australia, Perth, Australia, 1999.

(16) Frisch, M. J.; Trucks, G. W.; Schlegel, H. B.; Scuseria, G. E.; Robb, M. A.; Cheeseman, J. R.; Scalmani, G.; Barone, V.; Mennucci, B.; Petersson, G. A.; Nakatsuji, H.; Caricato, M.; Li, X.; Hratchian, H. P.; Izmaylov, A. F.; Bloino, J.; Zheng, G.; Sonnenberg, J. L.; Hada, M.; Ehara, M.; Toyota, K.; Fukuda, R.; Hasegawa, J.; Ishida, M.; Nakajima, T.; Honda, Y.; Kitao, O.; Nakai, H.; Vreven, T.; Montgomery, J. A., Jr.; Peralta, J. E.; Ogliaro, F.; Bearpark, M.; Heyd, J. J.; Brothers, E.; Kudin, K. N.; Staroverov, V. N.; Kobayashi, R.; Normand, J.; Raghavachari, K.; Rendell, A.; Burant, J. C.; Iyengar, S. S.; Tomasi, J.; Cossi, M.; Rega, N.; Millam, J. M.; Klene, M.; Knox, J. E.; Cross, J. B.; Bakken, V.; Adamo, C.; Jaramillo, J.; Gomperts, R.; Stratmann, R. E.; Yazyev, O.;

Austin, A. J.; Cammi, R.; Pomelli, C.; Ochterski, J. W.; Martin, R. L.; Morokuma, K.; Zakrzewski, V. G.; Voth, G. A.; Salvador, P.; Dannenberg, J. J.; Dapprich, S.; Daniels, A. D.; Farkas, Ö.; Foresman, J. B.; Ortiz, J. V.; Cioslowski, J.; Fox, D. J. *Gaussian 09, Revision C.01*; Gaussian, Inc.: Wallingford, CT, 2009.
(17) Marenich, A. V.; Cramer, C. J.; Truhlar, D. G. *J. Phys. Chem. B* **2009**, *113* (18), 6378−6396.
(18) Zhao, Y.; Schultz, N. E.; Truhlar, D. G. *J. Chem. Theory Comput.* **2006**, *2* (2), 364−382.
(19) Boese, D.; Martin, M. L. *J. Chem. Phys.* **2004**, *121*, 3405.
(20) Goerigk, L.; Grimme, S. *Phys. Chem. Chem. Phys.* **2011**, *13* (14), 6670−6688.
(21) Haram, S. K.; Quinn, B. M.; Bard, A. J. *J. Am. Chem. Soc.* **2001**, *123* (36), 8860−8861. Randriamahazaka, H.; Noël, V.; Chevrot, C. *J. Electroanal. Chem.* **1999**, *472* (2), 103−111.
(22) Andruniow, T.; Pawlikowski, M. *Chem. Phys. Lett.* **2000**, *321* (5−6), 485−490.
(23) Leong, C. F.; Faust, T. B.; Turner, P.; Usov, P. M.; Kepert, C. J.; Babarao, R.; Thornton, A. W.; , D. M. *Dalton Trans.* **2013**, *42*, 9831−9839.